In Situ Plasmonic Nanospectroscopy of the CO Oxidation Reaction over Single Pt Nanoparticles

N.B. When citing this work, cite the original published paper.

(article starts on next page)

ACS NANO

ARTICLE

# *In Situ* Plasmonic Nanospectroscopy of the CO Oxidation Reaction over Single Pt Nanoparticles

Su Liu, Arturo Susarrey Arce, Sara Nilsson, David Albinsson, Lars Hellberg, Svetlana Alekseeva, and Christoph Langhammer*

Department of Physics, Chalmers University of Technology, 412 96 Göteborg, Sweden

Ⓢ *Supporting Information*

ABSTRACT: The ongoing quest to develop single-particle methods for the *in situ* study of heterogeneous catalysts is driven by the fact that heterogeneity in terms of size, shape, grain structure, and composition is a general feature among nanoparticles in an ensemble. This heterogeneity hampers the generation of a deeper understanding for how these parameters affect catalytic properties. Here we present a solution that in a single benchtop experimental setup combines single-particle plasmonic nanospectroscopy with mass spectrometry for gas phase catalysis under reaction conditions at high temperature. We measure changes in the surface state of polycrystalline platinum model catalyst particles in the 70 nm size range and the corresponding

bistable kinetics during the carbon monoxide oxidation reaction *via* the peak shift of the dark-field scattering spectrum of a closely adjacent plasmonic nanoantenna sensor and compare these changes with the total reaction rate measured by the mass spectrometer from an ensemble of nominally identical particles. We find that the reaction kinetics of simultaneously measured individual Pt model catalysts are dictated by the grain structure and that the superposition of the individual nanoparticle response can account for the significant broadening observed in the corresponding nanoparticle ensemble data. In a wider perspective our work enables *in situ* plasmonic nanospectroscopy in controlled gas environments at high temperature to investigate the role of the surface state on transition metal catalysts during reaction and of processes such as alloying or surface segregation *in situ* at the single-nanoparticle level for model catalysts in the few tens to hundreds of nanometer size range.

KEYWORDS: *single-particle catalysis, single particle, plasmonic nanospectroscopy, CO oxidation, bistable kinetics, dark-field scattering spectroscopy, quadrupole mass spectrometry*
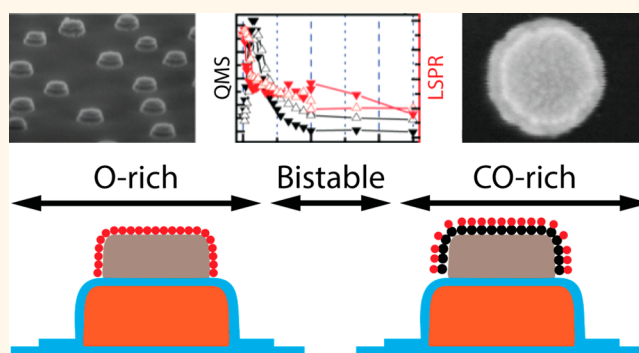
Studying individual nanoparticles is of high relevance in heterogeneous catalysis,[1−4] where they are widely used and where polydispersity in terms of size, shape, and grain structure is a general feature among them. This heterogeneity hampers the generation of a deeper under-standing for how these structural parameters affect catalytic activity since they, together with electronic and spillover interactions with the support,[5−8] directly control the catalytic performance. Assessing the state, activity, and selectivity of individual nanoparticles thus has significant potential to contribute to the development of efficient catalyst materials. Therefore, the characterization of single nanoparticles at *in situ* conditions is a major tour de force in catalysis, and significant efforts are invested in the development of the required experimental techniques.

To this end, plasmonic nanospectroscopy is an experimental concept that employs metal nanoparticles capable of manipulating light at the nanoscale, *via* electron oscillations known as localized surface plasmon resonance (LSPR).[9−11] Such plasmonic nanoantennas have been successfully used as nanoscopic probes of various processes including phase transitions,[11] biomolecule interactions and sensing,[12−14] metal hydride formation,[15] gas- and chemosensing,[10,16] and catalytic reactions.[17−21] In catalysis applications they can report directly on the catalyst nanoparticle surface or bulk state due to the intrinsically very high sensitivity of LSPR to surface and bulk changes.[11] One of the most appealing assets of the

plasmonic nanospectroscopy concept, when projected onto catalysis research, is the possibility to address *individual* nanoparticles in the 10−100s nm size regime, which is accessible to the enhanced precision of top-down nanofabrication that enables the preparation of controlled and precisely tunable model systems.[4,22−25] Notably, this single-nanoparticle resolution comes without principle restrictions on the surrounding medium; that is, both liquid and gas phase environments are accessible at ambient pressure or above.[6,13,19,26−31] Moreover, multiple individual nanoparticles can be addressed simultaneously using concepts such as hyperspectral imaging and derivatives.[32−35] This potentially offers similar insights as recently obtained by *in situ* X-ray absorption spectromicroscopy at a beamline[4,7] but with benchtop optical microscopy instrumentation for optical dark-field scattering spectroscopy.[36]

To date, the plasmonic nanospectroscopy concept has been successfully applied to study catalytic processes at the single-particle level at *in situ* conditions in the liquid phase, as introduced in the seminal paper by Novo *et al.*[19] Subsequent studies by various groups further diversified the concept[37] to, for instance, investigate the photocatalytic decomposition of lactic acid,[31] Au nanoparticle-catalyzed redox reactions between glucose and O$_2$,[38] hydrogenation of chemisorbed 4-NTP,[39] electron transfer rates from different nanoparticle facets,[40] spectroelectrochemistry,[41] and spillover effects to an oxide support.[6] However, while elegantly demonstrating the single-particle capabilities of plasmonic nanospectroscopy in catalysis, all these studies have been carried out in the liquid phase and at or close to room temperature. Thus, they leave unaddressed the important field of gas phase heterogeneous catalysis, which typically takes place at several hundred Kelvin at atmospheric pressure or above. Furthermore, all these investigations have in common that they solely rely on the plasmonic signal, that is, the spectral shift of the resonance peak as the readout. In other words, only the state of the catalyst nanoparticle itself (*e.g.*, charge or oxidation state)[19,40] or of the surrounding medium (*e.g.*, *via* spillover)[6] is reported, while the reaction products remain unanalyzed.

As a first step toward overcoming these limitations, we report an experimental concept and the corresponding setup that combines *in situ* single-particle plasmonic nanospectroscopy of catalyst nanoparticles with a gas phase catalytic flow reactor operating at up to 623 K and equipped with a quadrupole mass spectrometer (QMS) for the simultaneous quantitative analysis of reaction products from an adjacent ensemble (on the order of 10^9 particles) of nominally identical nanoparticles prepared by nanofabrication (Figure 1). This design enables the direct investigation of ensemble averaging effects in a single experiment since individual nanoparticles (LSPR) and a corresponding ensemble (QMS) can be probed simultaneously in the same experiment. To this end, we also note that for the detection of bioanalytes in the liquid phase both SPR[42] and LSPR[43] sensing setups have been combined with mass spectrometry, however, not simultaneously as done here.

As the second step we introduce a Au@SiO$_2$−Pt nanostructure design according to the indirect nanoplasmonic sensing[17,44] scheme, where a nanofabricated single Au plasmonic antenna observer, which is completely encapsulated in SiO$_2$ and closely adjacent to the active single Pt catalyst nanoparticle, boosts the total light-scattering signal of the structure and serves as optical transducer in the plasmonic
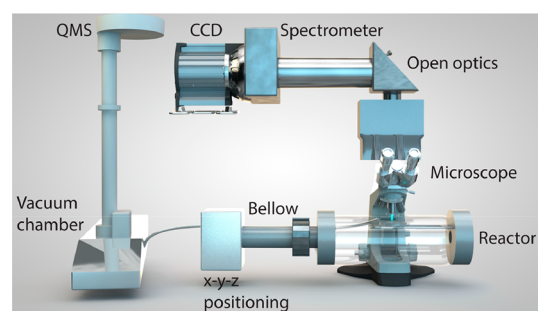

Figure 1. Overview of the setup that is centered on a flow-reactor tube made from glass. To enable dark-field scattering spectroscopy, the reactor tube is equipped with a flat 200 μm thick optical window. The flow reactor arrangement is mounted on the sample stage of an upright optical microscope. It is connected to a spectrometer equipped with a CCD camera to collect scattered light from (individual) catalyst nanostructures *via* a long-working-distance 50× dark-field objective and epi-illumination. It is also equipped with a gas inlet connected to mass-flow controllers for accurate control of reactant concentration and reactant flow. The quadrupole mass spectrometer (QMS) is mounted on a high-vacuum chamber that is connected to the flow reactor chamber *via* a stainless steel tube. To enable the QMS readout directly from the close vicinity of the nanofabricated sample surface, we use a glass capillary "sniffer" mounted inside the flow reactor. It acts as orifice leak and has a ∼5 μm opening. Its position can be accurately controlled *via* an x−y−z micrometer stage. To control sample temperature, the system is internally equipped with a flat ceramic carbon heater that serves as the sample holder for the nanofabricated model catalyst.

nanospectroscopy single-nanoparticle readout. This arrangement is necessary since most of the transition metal catalysts are poor light scatterers,[45] and it has the potential to enable studies of individual catalyst particles in the sub-10 nm size regime most relevant to industrial catalysis.[28,46,47] Here, we use nanofabricated ∼20 × 70 nm *polycrystalline* Pt nanoparticles as our model system to deliberately create sizable particle heterogeneity in terms of grain structure, defects, and surface faceting to demonstrate how such parameters impact reaction kinetics at the single-nanoparticle level.

As the third step and to demonstrate and benchmark our setup using these Au@SiO$_2$−Pt structures, we investigated the kinetic phase transition phenomenon and the corresponding bistable kinetics that have been reported for the carbon monoxide (CO) oxidation reaction both on single-crystal surfaces[48] and on nanofabricated Pt model catalysts.[22,48,49] As the main results obtained at atmospheric pressure conditions, we found that the reaction kinetics of simultaneously measured individual model catalyst nanoparticles are remarkably different and critically depend on their grain structure in terms of abundance of grains and of the corresponding surface faceting and that the superposition of the individual nanoparticle response can account for the significant broadening observed in the corresponding nanoparticle ensemble data.

RESULTS AND DISCUSSION

Our experimental setup (Figure 1; for a more technical drawing refer to Figure S1 in the Supporting Information, SI) comprises an upright optical microscope operated in dark-field epi-illumination mode. It is connected to a spectrometer equipped with a CCD camera, which is used to collect scattered light from (individual) plasmonic nanostructures *via*

a long working-distance 50× objective and thus enables both ensemble and single-particle plasmonic nanospectroscopy readout from a tailor-made catalytic reactor described below. Plasmonic nanospectroscopy relies on the fact that the LSPR frequency of a metal nanoparticle is very sensitive to minute changes on its surface or on a second nanoparticle in its close vicinity.[13,17,28,29] Using dark-field scattering spectroscopy, the induced change in LSPR frequency can be efficiently detected as a spectral shift of the peak maximum in the light-scattering spectrum of a single nanoparticle, with resolution high enough to detect single molecules.[35] In our setup focusing on catalysis applications, the nanofabricated plasmonic/catalytic sample is mounted on an inert flat ceramic carbon heater installed inside a glass flow reactor tube with 400 mm diameter, which we have equipped with a 1 in., 200 μm thin flat optical window to facilitate dark-field scattering spectroscopy readout from inside the reactor. It is also equipped with a gas inlet connected to mass-flow controllers for accurate control of reactant concentration. An active feedback loop controls the temperature of the sample up to 623 K *via* a thermocouple and a temperature controller. To facilitate the QMS readout directly from the nanofabricated sample surface, we use a glass capillary "sniffer",[50] which is mounted inside the flow reactor. Its position can be accurately controlled *via* an $x-y-z$ micrometer stage connected to the reactor by a stainless steel bellow. *Via* a stainless steel tube, the sniffer is further connected to a UHV chamber, on which the QMS is mounted. The opening of the glass capillary sniffer toward the sample is tuned to 5 μm using the method introduced by Kasemo.[50] In this way it effectively acts as orifice leak for local, fast-response gas sampling using the QMS by ensuring the necessary pressure drop from 1 atm inside the reactor to below the maximal operation pressure of the QMS, which is on the order of 10^{-6} mbar.

To initially validate the function of the setup, we benchmarked it with our earlier work on the kinetic phase transition that occurs during the hydrogen oxidation reaction over a Pt nanoparticle *ensemble* model catalyst due to bistable kinetics, which we had studied when introducing the indirect nanoplasmonic sensing concept.[17] The corresponding analysis of a very similar set of experiments using our combined plasmonic nanospectroscopy and QMS setup presented here is summarized and discussed in detail in the SI and Figures S2 and S3. As the first key result, it reproduces the insights obtained in our previous study using a traditional quartz-tube flow reactor setup and simple optical transmittance measurements.[17] As the second key result, it demonstrates the anticipated complementary of the optical and the QMS signals, that is, that the QMS reports the catalyst activity of the nanofabricated model catalyst ensemble and that the plasmonic nanospectroscopy optical signal directly reports the catalyst surface state, as identified by the observed coincidence of the highest reaction rate and change of the catalyst surface state at the kinetic phase transition (Figure S2c).

To enable single-particle plasmonic nanospectroscopy from a Pt model catalyst, which by itself is a weak light scatterer,[45] we want to place it closely adjacent to an inert plasmonic nanoanetanna "observer" in order to enhance the total scattering cross-section of the system. However, in contrast to the earlier implementations of this concept,[26,28,51] here we also have to consider the high operating temperature of our system and thus develop a means to spatially separate the catalyst from the Au nanoantenna to prevent alloy or intermetallic phase formation between the two.[52,53] For this purpose, we further tailored our hole−mask colloidal lithography nanofabrication approach (see Methods for details), to enable the chemical vapor deposition of a thin SiO_2 layer *through* the nanofabrication mask that encapsulates the *entire* Au nanoantenna before the growth of the Pt catalyst nanoparticle (Figure 2a). In this way, due to the self-alignment, it becomes possible to grow the catalyst exclusively on top of the nanoantenna sensor, while simultaneously still completely encapsulating the underlying Au nanoantenna. This results in a Au@SiO$_2$−Pt hybrid nanostructure with combined sensing (*via* the Au nanoantenna) and catalytic (*via* the Pt) function (Figure 2b−d). Furthermore, since different types of separating layers, as well as catalyst particle materials, can be grown in this way, our approach is generic and can be easily expanded to other catalyst systems to tailor the catalyst formulation in a modular fashion.

To test the thermal and chemical stability of the Au@SiO$_2$−Pt nanostructures used here, we thermally annealed them at 623 K in 3% H_2 + 3% O_2 for 2 h and exposed them to reaction environment for the CO-oxidation reaction (3% CO + 3% O_2) at 623 K for 0.5 h and in Ar carrier gas. The corresponding scanning electron microscopy (SEM) analysis reveals their structural integrity, as well as the anticipated recrystallization of the Pt (Figure 2e−g). Furthermore, comparing a representative single-particle scattering spectrum of such a nanoarchitecture after the thermal and reaction treatment (Figure 2h) with a corresponding finite-difference time-domain (FDTD) simulation (Figure 2i depicts the used simulation scheme) reveals good agreement and thus further corroborates both the integrity of the nanostructure and the anticipated coupling between the two metal elements, essential for the indirect sensing principle.

To further characterize the Pt model catalyst nanoparticles, we performed transmission electron microscopy (TEM) analysis. However, since the entire Au@SiO$_2$−Pt hybrid structure would be too thick for TEM imaging, as well as would lead to convoluted images due to the stacked Au and Pt particles, we nanofabricated *analogous* Pt model catalyst nanoparticles (*i.e.*, without Au underneath) with the same size on a TEM membrane and treated them in the same way as the real sample at the reaction conditions described above. The corresponding TEM images of representative Pt nanoparticles reveal the formation of mainly polycrystals with various numbers of grains (Figure 3a). Further resorting to our earlier detailed characterization of the grain structure in equivalently nanofabricated Pd nanoparticles using transmission Kikuchi diffraction (TKD), we conclude that each nanoparticle has its distinct and unique grain structure with different grain orientation (*cf.* Figure 5 in ref 35) and multiple surface facets exposed by the different grains (*cf.* Figure S17 in ref 35). Hence they fulfill the desired criterion to serve as single-particle model systems for structurally distinctly different catalyst nanoparticles.

As the final characterization step of the Au@SiO$_2$−Pt hybrid nanostructures to ensure that the SiO$_2$ layer indeed encapsulates the Au nanoantenna and prevents direct contact between Au and Pt elements even at reaction conditions, we carried out X-ray photoelectron spectroscopy (XPS) analysis (Figure 3b). It reveals that the distinct characteristic Pt 4f peaks are preserved even after the reaction treatment and thus corroborates that no mixing with the Au nanoantenna has occurred.
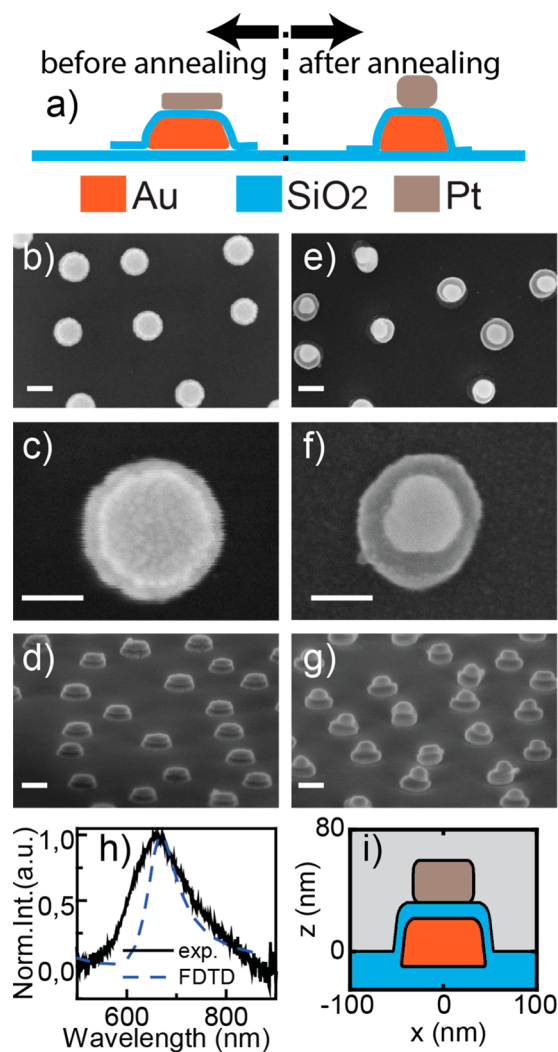
Figure 2. Characterization of nanofabricated Au@SiO$_2$–Pt hybrid nanostructures with combined sensing and catalytic function. (a) Schematic depiction of the structures that are composed of a Au nanoantenna (20 nm thickness) encapsulated in a 10 nm thin silica layer with a nanofabricated Pt model catalyst nanoparticle on top. (b) Top-view (scale bar: 100 nm), (c) top-view zoom-in (scale bar: 50 nm), and (d) side-view (scale bar: 100 nm) SEM images of such nanoarchitectures directly after deposition of the respective layers and prior to any thermal treatment or catalytic reaction. SEM images taken after thermal annealing under reaction conditions described in the text: (e) Top-view (scale bar: 100 nm), (f) top-view zoom-in (scale bar: 50 nm), and (g) side-view (scale bar: 100 nm). Note the structural integrity of the nanoarchitecture and its components and the change in dimensions of the Pt catalyst due to recrystallization. (h) Representative single-particle scattering spectrum of the thermally treated Au@SiO$_2$–Pt nanostructure displayed in (f) together with the corresponding finite-difference time-domain (FDTD) simulation. (i) Graphic illustration of the used FDTD simulation scheme assuming the following nanostructure dimensions to mimic the Au@SiO$_2$–Pt architecture after annealing: Au disk: 90 nm × 27 nm, SiO$_2$ thickness: 10 nm, Pt nanoparticle: 65 nm × 28 nm.

To generally characterize the catalytic properties of the Au@SiO$_2$–Pt hybrid nanostructures, we first performed *ensemble*-type experiments using the oxidation of carbon monoxide (CO + 1/2 O$_2$ → CO$_2$) over Pt as the model reaction.[54] Specifically, we put our focus on the phenomenon of kinetic phase
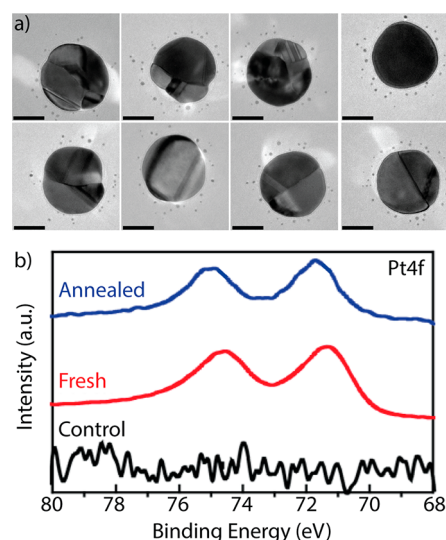

Figure 3. TEM and XPS sample characterization. (a) TEM images of representative Pt nanoparticles after high-temperature annealing and reaction condition treatment. (b) High-resolution XPS spectra in the Pt 4f spectral region of a fresh and a reaction-treated Au@SiO$_2$–Pt sample, as well as of a Au@SiO$_2$ (*i.e.*, no Pt on top) control. As the main observation, we note that no significant changes in terms of intensity or binding energy take place for the Pt 4f lines (the small difference observed is a consequence of surface charging effects due to the used oxidized silicon substrate), corroborating that no Pt–Au alloy/intermetallic phase is formed, and thus that the SiO$_2$ encapsulation layer does not deteriorate during reaction.

transitions and the corresponding reported kinetic bistabilities, that is, the existence of two stable kinetic regimes that may coexist for a given set of reaction conditions, which has been reported for the CO oxidation reaction both on nanofabricated Pt model catalysts[22] and on single-crystal surfaces.[48] In the present case, as illustrated schematically in Figure 4, this means that at low relative CO concentration, $\alpha^{CO} = [CO]/([CO] +$
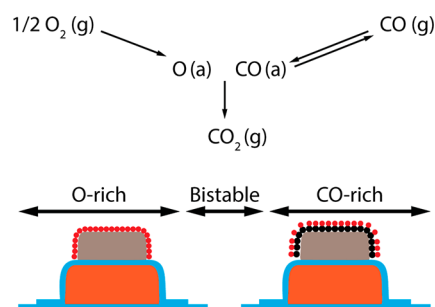

Figure 4. Schematic depiction of the CO oxidation reaction and the three kinetic regimes. The top scheme illustrates the key steps of the CO oxidation reaction over a Pt catalyst, involving dissociative adsorption of molecular oxygen, nondissociative adsorption of CO, and formation and desorption of the CO$_2$ reaction product. The bottom scheme depicts the origin of the bistable kinetics at the interface between the O-rich and CO-rich reaction regimes. In oxygen excess, the surface of the Pt nanoparticles is mainly covered by dissociated chemisorbed oxygen (O). By increasing the CO concentration in the feed the reaction rate increases until a critical CO concentration is reached and a so-called kinetic phase transition occurs to a state where CO predominantly covers the surface.

[O_2]), or in other words in oxygen excess, the surface of the Pt nanoparticles is mainly covered by dissociated chemisorbed oxygen (O). In this regime the reaction rate is high and almost proportional to the supplied CO concentration in the feed, since the influence of O on the sticking probability of CO is small. Accordingly, the reaction rate increases until a critical CO concentration is reached, and the kinetic phase transition[49] occurs to a new state where the surface is predominantly covered by CO. In this state the reaction rate is significantly reduced since the adsorbed CO molecules effectively block or "poison" the chemisorption of O_2 and thus limit the supply of O to form CO_2. This asymmetry in terms of poisoning in the O- or CO-covered surface regimes can give rise to the coexistence of two stable kinetic states and thus hysteresis in obtained reaction rates, depending on the initial surface condition. Typically, at higher temperatures, the coexistence region is narrowing and eventually disappears due to the increasing CO desorption rate, which ultimately eliminates the poisoning effect.[22,49]

To explore this phenomenon with our setup and for the Au@SiO$_2$−Pt model catalyst, we varied α^{CO} in the reactant flow from a CO-rich to an O_2-rich condition and back again, while keeping the total reactant concentration ([CO] + [O_2]) constant at 9% in Ar carrier gas. Simultaneously, we continuously recorded both the CO_2 partial pressure in the reactor via the QMS and the plasmonic nanospectroscopy peak position signal, λ, via the dark-field scattering spectroscopy readout from a sample area comprising ca. 5000 Au@SiO$_2$−Pt nanostructures (Figure 5a). The sample temperature was set to 503 K. A complete α^{CO} up- and down-sweep together with the corresponding QMS and λ response are summarized in Figure 5b. We observe a maximum in the reaction rate at a critical reactant mixture α^{CO}_{cr} = 0.04−0.05, at which the optical λ signal exhibits a distinct change in trend. Since the α^{CO} steps displayed in Figure 5b are nonlinear in magnitude, this becomes clearer in Figure 5c, where the QMS and plasmonic nanospectroscopy data (now expressed as the shift of the LSPR scattering peak position, $\Delta\lambda$, with respect to the first taken data point at $t = 0$) are plotted as a linear function of α^{CO}. Both for the α^{CO} up- and down-sweep, $\Delta\lambda$ is essentially constant for $\alpha^{CO} < \alpha^{CO}_{cr}$ and then rapidly spectrally blue-shifts for $\alpha^{CO} > \alpha^{CO}_{cr}$, to reach a steady-state value beyond $\alpha^{CO} \approx 0.2$. The reaction rate obtained by the QMS and expressed as CO_2 partial pressure in the chamber exhibits a distinct maximum that coincides with the onset of the blue-shift of $\Delta\lambda$.

It is now interesting to further discuss these data in the context of the bistable reaction kinetics introduced above. To this end, first, we observe hysteresis between α^{CO} up- and down-sweeps in both the QMS and the $\Delta\lambda$ response, in good agreement with Joháne et al.,[22] who investigated the bistability phenomenon using molecular beam experiments on nanofabricated Pd model catalysts over a wide size range (2−500 nm). They found a distinct particle size dependence of the hysteresis as a consequence of the interplay between a higher abundance of defects on smaller particles and fluctuations between the two kinetic reaction regimes. Second, as predicted by theory,[49] we also observe increased or decreased hysteresis width at lower and higher reaction temperature, respectively (Figure S4), in both the QMS and plasmonic nanospectroscopy response. This is the consequence of CO poisoning being less severe at higher temperature due to enhanced CO desorption. Third, we notice the excellent agreement in global trend between QMS
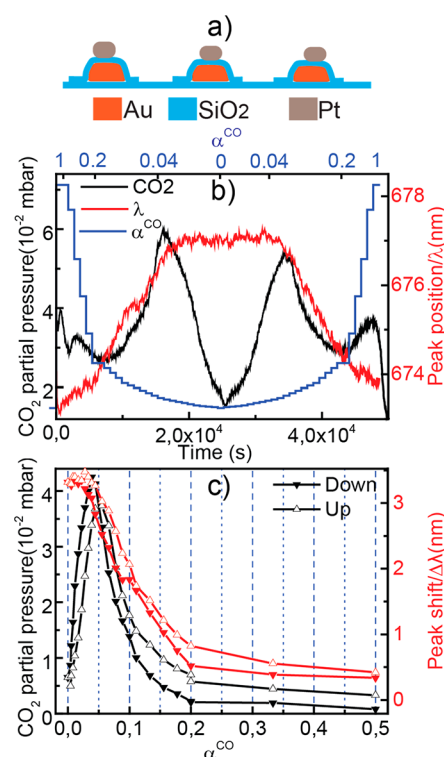

Figure 5. Correlated ensemble plasmonic nanospectroscopy and mass spectrometry for CO oxidation over Pt. (a) Schematic cross-section of the used array of Au@SiO$_2$−Pt nanostructures. (b) CO_2 partial pressure measured by the QMS together with the corresponding spectral position of the plasmonic scattering peak readout, λ, obtained during reaction at 503 K. The data are plotted as a function of the relative CO concentration in the gas flow, α^{CO} = [CO]/([CO] + [O_2]), at a constant total reactant concentration of 9% in Ar carrier gas. During the experiment, α^{CO} is swept from 1 to 0 and back to 1, in steps of 0.006 close to α^{CO}_{cr} and in steps of 0.16 otherwise. As the key feature, we observe that a distinct change in trend of the plasmonic nanospectroscopy signal, λ coincides with the maximum in CO_2 partial pressure measured simultaneously by the QMS at α^{CO}_{cr} = 0.04 ± 0.006. (c) The same data as in (b) but plotted as a function of the α^{CO} value for 0 < α^{CO} < 0.5. Both for the α^{CO} up- and down-sweep, the plasmonic peak shift, $\Delta\lambda$, is essentially constant for $\alpha^{CO} < \alpha^{CO}_{cr}$ and then rapidly blue-shifts for $\alpha^{CO} > \alpha^{CO}_{cr}$, to reach a steady-state value beyond $\alpha^{CO} \approx 0.2$, where the catalyst activity is essentially zero, as seen from the QMS signal. This is the signature of the kinetic phase transition from a predominantly O-covered to a reduced CO-covered surface.

signal and $\Delta\lambda$ response in the CO-rich surface regime and the contrasting essentially constant $\Delta\lambda$ signal in the O-rich surface regime, despite a significant change in reaction rate. This indicates that the plasmonic nanospectroscopy signal, $\Delta\lambda$, directly reports the surface state of the catalyst at in situ conditions, which at the kinetic phase transition switches from an essentially constantly O-covered (and thus presumably oxidized/reconstructed[55−57]) to a mainly CO-covered surface. However, due to the relatively high temperature of our experiment, the CO coverage depends more strongly on the absolute α^{CO} value than the O coverage (for which the higher temperature rather stabilizes any oxide,[55] if formed), since it dictates the equilibrium with CO in the gas phase.[49] Furthermore, it has been demonstrated in a recent combined photoemission electron microscopy (PEEM) and QMS study[58] of the local catalytic ignition during CO oxidation
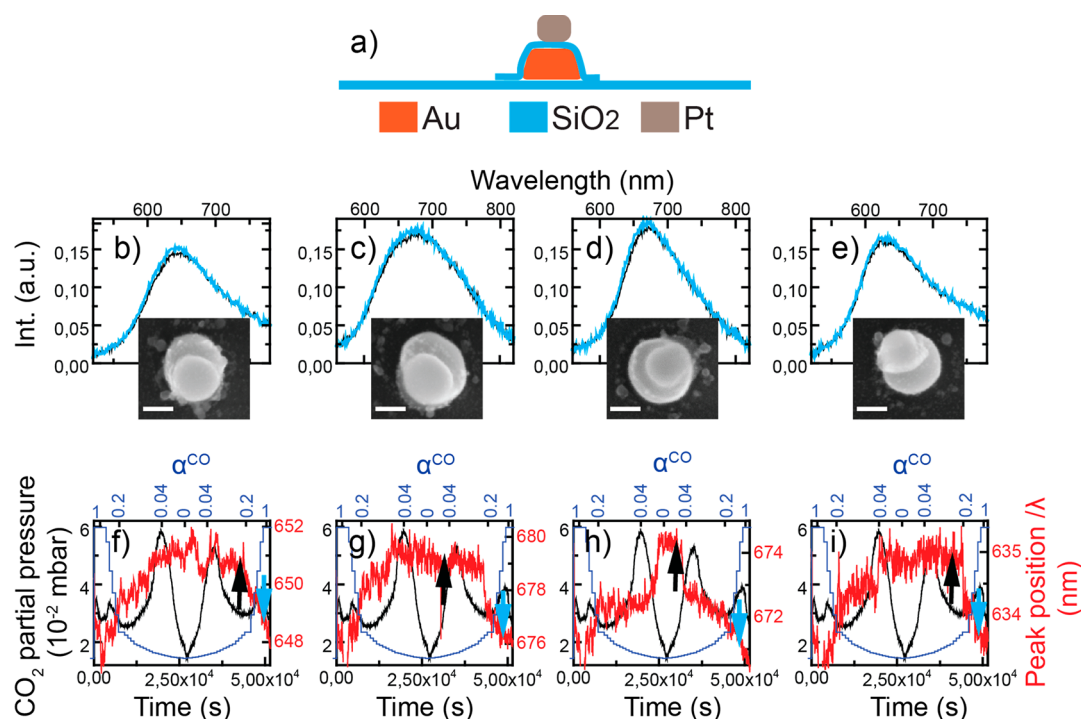
Figure 6. Simultaneous single-particle plasmonic nanospectroscopy and ensemble mass spectrometry for CO oxidation over Pt. (a) Schematic cross-section of the used single $Au@SiO_2$–Pt nanostructures. (b−e) Dark-field scattering spectra of the four nanostructures simultaneously under study together with corresponding SEM images (scale bar 50 nm). The scattering spectra were taken for a surface in the CO-covered state (blue) and in the oxidized O-covered state (black). Note the difference in response for the two chemical states. (f−i) Combined plots for scattering peak position λ obtained by plasmonic nanospectroscopy (red) for each nanoparticle shown in (b)−(e) and the overall CO_2 partial pressure (black) in the reactor measured with the QMS, acquired during a 15 h experiment sweeping α^{CO} (blue) from 1 to 0 and then back to 1. We note a different but completely reversible single-nanoparticle response. The black and blue arrows indicate where along the experimental sequence the spectra shown in (b)−(e) were taken.
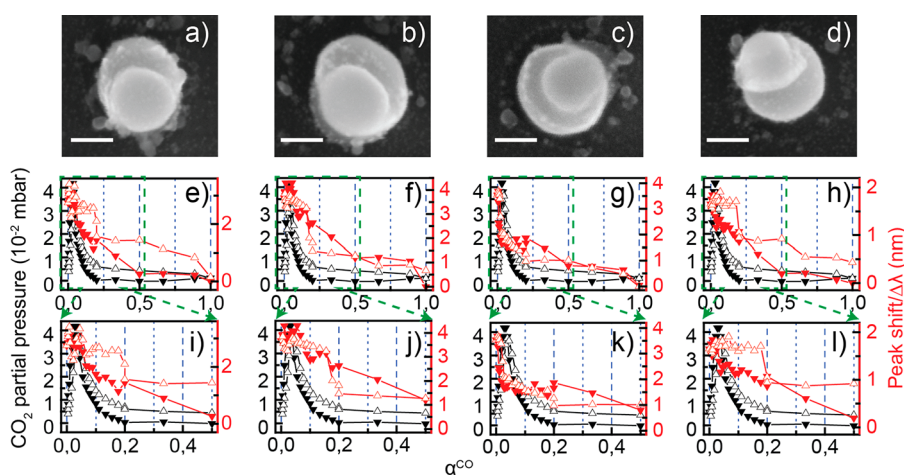

Figure 7. Simultaneous single-particle plasmonic nanospectroscopy and ensemble mass spectrometry for CO oxidation over Pt at 503 K. (a−d) SEM top view micrographs of the single $Au@SiO_2$–Pt nanostructures used in the experiment depicted in Figure 5. The scale bar is 50 nm. (e−h) CO_2 partial pressure measured by the QMS (black) and correlated single-particle plasmonic nanospectroscopy signal (red) as a function of α^{CO} up- and down-sweep (upward- and downward-pointing triangles, respectively). The plots are derived based on the raw data depicted in Figure 6 by averaging the QMS signal and the peak shift, $\Delta\lambda$, for each of the four particles over the 15 min long α^{CO} steps during the sweep. (i−l) Zoom-in on the kinetic phase transition region (α^{CO} = 0−0.5) to highlight the quite different nature of the transition on the different nanoparticles.

on low-index Pt surfaces present on a polycrystalline Pt foil that the global QMS CO_2 signal obtained from the entire foil (*cf.* Figure S1 in ref 58) is significantly "smeared" along the CO partial pressure axis (which is equivalent to α^{CO} used here) compared to the PEEM intensity measured from single grains with different surface termination ((111), (100), and (110))

within the foil. Using the PEEM intensity together with density functional theory (DFT) calculations the authors also showed that the local kinetic phase diagrams for individual Pt grains in the foil vary significantly depending on their index (*cf.* Figure 3 in ref 58). Hence, the smearing in the global QMS signal is a consequence of the superposition of the local kinetics of all

grains with a different index present in the foil. In analogy, we argue that the same mechanism is in play in our system since (111), (100), and (110) facets are the dominant surfaces of nanofabricated Pt nanoparticles after annealing, with significant variations in terms of their relative abundance from particle to particle (see Figure 5 in ref [59]). Hence, the relatively gradual change of $\Delta\lambda$ across the kinetic phase transition and thus the corresponding gradual change of CO surface coverage measured in our experiment (Figure 5c) are the consequence of the ensemble averaging over *ca.* 5000 nanoparticles with different facets that exhibit kinetic phase transitions at different α^{CO}.

To enable single-particle plasmonic nanospectroscopy during CO oxidation reaction conditions, we prepared a sample comprising three different areas (Figure S5). In the center is a 4 × 8 mm area with the standard nanoparticle surface coverage of *ca.* 15% obtained by HCL nano-fabrication,[60] including a small region close to the edge (*ca.* 5% of the total surface area) with a particle coverage low enough (*i.e.*, particle−particle distances larger than the diffraction limit) for single-particle plasmonic nanospectro-scopy (Figure 6a; see Methods for details of the nano-fabrication). To the left and right is a 4 × 8 mm area with identical Au@SiO$_2$−Pt nanostructures but at *ca.* 40% surface coverage to provide enough reaction product for detection by the QMS. In total this means that about 10^9 particles are averaged for the QMS readout. Focusing optically on the low-density area of this sample arrangement, we aligned a set of four individual particles within the spectrometer slit, to track their optical response simultaneously and independently (Figure 6b−e). These four particles lie within an area of 35 μm × 6 μm (Figure S 5d), which ensures that they experience the same conditions. Using this arrangement, we executed the same experiment as for the ensemble case discussed above, sweeping α^{CO} (9% total reactant concentration in Ar carrier gas at a constant flow rate of 100 mL/min) in a stepwise fashion in 0.16 and 0.006 α-units per step for $\alpha^{CO} > 0.2$ and $\alpha^{CO} < 0.2$, respectively, from a CO-rich to a O$_2$-rich condition and back again. The sample temperature was set to 503 K, and we simultaneously monitored the peak position, λ, of the scattering spectra of the four catalyst nanoparticles and the CO$_2$ reaction product from the corresponding ensemble (Figure 6f−i and Figure S6 for a contour plot of the entire spectral evolution).

To further analyze these raw data and decrease the noise level, we averaged the QMS and $\Delta\lambda$ signals for each of the four particles (Figure 7a−d; for an identical second data set measured at 533 K see Figure S7) over each 15 min long α^{CO} step and plotted the corresponding averaged $\Delta\lambda$ values as a function of α^{CO} for both increasing and decreasing α^{CO} (Figure 7e−h and i−l for zoom-in on a narrower α^{CO} range). We immediately notice that the overall response looks quite different for the four nanoparticles, which were measured all at the same time. Hence, we can ascribe these differences to their individual response. For example, defining the largest spectral shift between two data points as the kinetic phase transition, we find that it occurs at values ranging from 0.0044 to 0.2 for the α^{CO} up-sweep on the different particles. At the same time, for the α^{CO} down-sweep, the difference between particles is smaller. Also hysteresis, however with different width, occurs between the α^{CO} up- and down-sweeps for all four particles. These observations are in line with our arguments put forward above,[58] that is, that different nanoparticles exhibit variations in terms of the relative abundance of the dominant surface facets,[59] as well as in terms of grain boundaries and related defects (Figure 3). Consequently, they are expected to exhibit the kinetic phase transition at different α^{CO}, in agreement with what we observe in our experiments. Looking even more in detail and comparing the single nanoparticle $\Delta\lambda$ response with the one from the ensemble (*cf.* Figure 5c), we note that for the single nanoparticles distinct steps in $\Delta\lambda$ and thus in reactant surface coverage occur at the kinetic phase transition, whereas such steps are absent in the ensemble data. Also this observation is thus in line with the main hypothesis of our work, namely, that single-nanoparticle experiments enable insights beyond ensemble averaging, and it demonstrates that the rather smeared out transition in reactant surface coverage reported by $\Delta\lambda$ from the ensemble is the consequence of averaging the rather sharp transitions of the individual nanoparticles, which may occur across a range of α^{CO}, dictated by the particle-specific abundance of grains, defects, and certain surface facets. In this sense, our results for the individual nanoparticles are also well in line with the PEEM study of the polycrystalline Pt foil, for which the kinetic phase transition is rather continuous at the global level and a distinct step at the level of the individual grain with dimensions on the order of 100 μm (rather than 100 nm as in our case here).[58] These observations thus show how the reaction kinetics of simultaneously measured individual model catalyst nano-particles critically depend on their grain structure and how such information can be obtained at *in situ* conditions (compared to the to-date used surface science techniques operating at (ultra)high-vacuum conditions such as PEEM[58]) using plasmonic nanospectroscopy based on a benchtop-type experimental setup comprising an optical microscope and a traditional catalytic flow reactor operating at atmospheric pressure.

CONCLUSIONS

In summary, we have presented an experimental setup that combines *in situ* gas phase single-particle plasmonic nano-spectroscopy of individual catalyst nanoparticles with mass spectrometry on a corresponding nanoparticle ensemble in one and the same experiment. In the current design, the system operates at atmospheric pressure and is compatible with temperatures of up to 623 K. We have also developed a nanofabrication method for the crafting of Au@SiO$_2$−Pt hybrid nanostructures to achieve combined sensing function (*via* an oxide-encapsulated Au nanoantenna) and catalytic function (*via* a single Pt model catalyst particle on top) within the same structure, to enable plasmonic nanospectroscopy based on the indirect sensing principle at the single-nanoparticle level and in harsh conditions. To demonstrate the capabilities of our setup, nanostructures, and the general experimental approach, we used ∼20 × 70 nm polycrystalline Pt nanoparticles as the active part in the Au@SiO$_2$−Pt hybrid nanostructure model system, since they offer maximized particle heterogeneity in terms of defects and surface faceting at the single-nanoparticle level. We then applied these structures to investigate the bistable kinetics of the CO oxidation reaction over Pt. As the key results we first found that a characteristic kinetic phase transition can be resolved both at the ensemble and single catalyst nanoparticle level as a distinct spectral shift in the plasmonic nanospectroscopy readout and that it occurs at the highest reaction rate identified by the simultaneous QMS readout. This is in agreement with

theory and experimental data obtained using surface science techniques in the corresponding literature. Second, we found that the bistable reaction kinetics and the signature of the kinetic phase transition of simultaneously measured individual model catalyst nanoparticles critically depend on their grain structure, defects, and surface faceting and that the superposition of the individual nanoparticle response induces a significant broadening and smearing in the corresponding kinetic response of a nanoparticle ensemble. This highlights that our experimental approach, which enables studies of catalysts *both* at the individual nanoparticle level and at the ensemble level in the same system, has the potential to shed light on the role of local catalyst design parameters, such as loading, particle size, shape, and dispersion, as well as metal–support interactions, on reaction kinetics, and how ensemble averaging limits our insights in this respect. To this end, we also briefly summarize the main challenges with the presented approach and developed instrumentation: (i) To maintain the particles of interest in focus during the (typically very long) experiments, in particular at elevated temperature due to thermal expansion effects. Here we predict that the implementation of active focus control solutions will lead to significant improvements in this respect.[61] (ii) To obtain enough product from the reaction over these nanofabricated model catalysts to enable online QMS detection. Here the use of microreactors with significantly smaller volumes and thus QMS detection limits could provide interesting solutions.[62]

In a wider perspective, we predict that our instrument as such, due to the available high temperature and controlled gas environment, and the experimental concept in particular, due to its high sensitivity, will enable single-particle investigations of, for example, the catalyst state during rate oscillations[48] since LSPR is highly sensitive to nanoparticle shape.[63,56] Furthermore, it will enable studies of the role of the surface state on noble metal catalysts such as Cu and Ag (which themselves are highly plasmonically active) during reaction, of thermally induced nanoalloy formation where LSPR will report on the concurrent change of the complex dielectric function as alloy formation occurs,[52,64] or of the annealing and segregation of alloy components in bimetallic catalysts under reaction conditions *via* LSPR interface damping effects that occur upon enrichment of a certain element at the surface.[65−67]

METHODS

Experimental Setup. The main parts of the experimental setup used in this work consisted of a in-house-built transparent flow reactor, a quadrupole mass analyzer (Leda Mass Vacscan), a modified Nikon upright microscope (Eclipse LV150N), and a spectrometer/CCD system (Andor Shamrock 193i spectrograph and Andor Newton 920 CCD camera), as shown schematically in Figure 1 and in detail in Figure S1 in the SI. The central part of the flow reactor is a KF40 Duran glass tube (Hositrad), with a round, 25 mm diameter flat borosilicate optical window of 0.2 mm thickness welded in the center to allow collection of images and spectra of individual nanoparticles through the microscope objective in dark-field mode. The reactor is sealed using CF vacuum flanges and Viton O-ring sealed KF flanges, and it operates at atmospheric pressure. Reactants diluted in Ar carrier gas are introduced to the reactor through a gas inlet tube welded onto one of the flanges. The gas flow rate and composition are controlled by a set of mass flow controllers (Bronkhorst Low-ΔP-flow and EL-flow). The gas outlet is located on the opposite side of the flow reactor to maintain equilibrium plug-flow conditions during the reaction. An in-house-built stainless steel sample holder is mounted inside the reactor tube and equipped with a ceramic resistive heater

(Momentive HT01) onto which the sample is clamped. The sample temperature is controlled by a power supply (Instek GW GPS-1850) and a temperature controller (Eurotherm 3216) *via* a thermocouple-controlled feedback loop to maintain a constant temperature. The latter also prevents defocusing of the sample image during an experiment, which otherwise is induced by thermal expansion and contraction of the sample holder. To enable the mass spectrometric readout, the QMS glass capillary orifice "sniffer" is mounted at the end of the gas transfer line (6.0 mm stainless steel Swagelok tube) to allow only a small and controlled amount of gas leakage into the mass analyzer chamber. The glass capillary orifice was fabricated by inserting the tip of a borosilicate glass tube (2/0.1 mm outer/inner diameter, Hilgenberg) in a propane−oxygen flame in order to shrink the inner diameter to a few micrometers. A detailed description of this method can be found in ref 50. The gas leak rate through the orifice is around 2×10^{-4} mbar s^{-1}. With such a leak rate, the pressure inside the QMS analyzer chamber stays below about 6.3×10^{-6} mbar, which guarantees proper operation of the QMS. Such an orifice design enables efficient molecular flow of the gas from the reactor to the QMS analyzer chamber through the transfer line, and thus a fast response time can be achieved. The gas transfer line outside of the reactor and the QMS analyzer chamber are maintained at 385 K to prevent water condensation.

Mass Spectrometry. The QMS is controlled using a customized LabVIEW control program. All QMS raw data were measured as ion current of the corresponding gas. Since ≥91% of the gas inside the reactor consists of Ar, the Ar partial pressure (P_{Ar}) is roughly estimated as being the same as atmospheric pressure (1013.25 mbar). The partial pressure of reactants or product, P_i, was calculated in mbar by comparison with the Ar signal according to the equation

$$P_i = \frac{I_i}{I_{Ar}} \times 1.27 \div S_i \times 1013.25 \tag{1}$$

where I_i and I_{Ar} are ion currents of gas species i and Ar measured directly by the QMS and S_i is the relative sensitivity factor (RSF) of the quadrupole mass analyzer for species i. All shown QMS data are corrected for any background recorded from a control sample without Pt during an identical experimental sequence to the real experiment.

Dark-Field Scattering Spectroscopy. White light from the microscope lamp (Nikon LV-HL50W LL) is used to illuminate the sample, which is mounted inside the reactor close to the optical window, in dark-field mode through the objective (50× Nikon Plano LWD). Scattered light from the sample is collected in a backscattering mode using the objective and then directed toward the entrance slit of the spectrograph through a pair of identical 2 in. plano-convex lenses (f = 150 mm, Thorlabs). For single-particle measurements, the sample surface was first imaged at the zero grating position with the spectrometer slit fully open (2500 μm). After subsequently aligning a group of suitable nanoparticles along the center of the slit, the width of the slit was reduced to 450 μm to exclude multiple nanoparticles from being recorded on the same position along the y-axis of the CCD chip. The grating of the spectrograph (150 lines/mm, blaze wavelength 800 nm) was then centered at a suitable wavelength around 600−650 nm to acquire a dark-field scattering spectrum from the scatterers on the sample aligned within the slit of the spectrograph in the spectral imaging mode. Normalized scattering spectra I_{sc} from individual particles were thus obtained as a function of wavelength λ using the relation $I_{sc}(\lambda) = (S - D)/CRS$, where S is the collected signal from an integrated area with nanoparticle, D is the signal from the nearby area without nanoparticle (dark signal for background correction taken from an area with identical pixel width but without particles), and CRS is the signal collected from the diffuse white certified reflectance standard bright reference sample (Labsphere SRS-99-020). CRS is used in order to correct the signal for the lamp spectrum. The acquisition time for each spectrum was 10 to 15 s depending on the brightness of the particle. The obtained single-particle scattering spectra were fitted with a Lorentzian function (±75 nm from the peak position) to derive information about the temporal evolution of the peak position.[68]

For scattering measurements from nanoparticle ensembles, the slit width of the spectrometer was reduced to 100 μm to prevent saturation of the CCD sensor chip. To calculate normalized scattering spectra I_{sc}, the background signal D was collected from a blank substrate without any particles, under the same conditions as when the signal S was collected. The same CRS as in single-particle measurements was used for spectrum correction. Peak position was extracted using the same fitting procedure as in single-particle measurements.

Sample Nanofabrication. The Au@SiO$_2$–Pt nanostructures were fabricated on a thermally oxidized silicon substrate (100 nm oxide thickness) using a tailored variant of the hole–mask colloidal lithography (HCL) method that is described in detail elsewhere.[60] The main new step in the present nanofabrication route is the growth of a 10 nm thin SiO$_2$ layer *through* the nanofabrication mask generated using the standard HCL process, encapsulating a plasmonic nanoantenna particle grown before. The key step enabling this through-mask sputtering without compromising the final lift-off step is a prolonged oxygen plasma etch (90 s, 50 W, 250 mTorr, Plasma-Therm Batchtop RIE 95m) to create a significant underetch in the poly(methyl methacrylate) (PMMA) resist of the mask after the polystyrene bead tape-stripping step. After this plasma etch, the SiO$_2$ encapsulation was grown in an Oxford Plasmalab 100 inductively coupled plasma 180 at room temperature with a base pressure of 3×10^{-7} Torr and a deposition rate of 2.75 Å/s. The Au nanoantennas, which were grown using e-beam evaporation (Lesker PVD 225, base pressure of 5×10^{-7} Torr, 1.5 Å/s deposition rate), have nominal dimensions of 110 ± 10 nm in diameter and 20 nm in height. After encapsulation in the 10 nm SiO$_2$ shell, the Pt catalyst nanoparticle was then evaporated on top (Lesker PVD 225, base pressure of 5×10^{-7} Torr, 1.5 Å/s deposition rate), also still through the hole–mask, at a nominal thickness of 10 nm. A control sample was fabricated following the same recipe except for omitting the last step that evaporates the Pt catalyst. Finally, lift-off was used to remove the PMMA resist and all metal layers by step-by-step sonication in mr-Rem 700 (Microresist Technology GmbH), isopropyl alcohol, and acetone. It is important to note that the single-particle region of 5% coverage was formed due to faster drying at the edge when blow-drying after drop-casting a polystyrene (PS) solution onto the substrate. To increase coverage from 15% to 40%, 0.1 mmol of NaCl was added to the PS solution to reduce interparticle repulsion and thus particle density.[69]

CO Oxidation Experiments on Pt Catalyst Nanoparticle Ensemble. Prior to sweeping α^{CO} in the kinetic phase transition experiments, the sample was exposed to 20 cycles of alternating 9% CO (6.0 purity in Ar) and 9% O$_2$ (6.0 purity in Ar) pulses of 15 min duration, followed by a 1 h pulse of 9% CO, in order to activate the catalyst and reach a stable optical signal. During this treatment, the sample temperature was kept at 553 K. For the α^{CO} sweep, the temperature was kept constant at the set value, and the sample was exposed to a constant total reactant concentration [CO + O$_2$] of 9%, at a constant flow rate of 100 mL/min. A scattering spectrum was simultaneously collected every 60 s using an integration time of 0.1 s and 10 accumulations for the CCD. With the QMS, the ion currents of CO, CO$_2$, air/N$_2$, O$_2$, and Ar inside the reactor were continuously measured at a mass value of 28, 44, 14, 32 and 40, respectively, with a time resolution of 5 s. The QMS was operated in SEM mode. To subtract the CO$_2$ background signal, measurements on a control sample without Pt under the exact experiment conditions were also carried out at corresponding temperatures. The CO$_2$ QMS signal shown in this article for both ensemble and single-particle experiments is corrected by subtracting the CO$_2$ signal from the sample with Pt from the control sample without Pt catalyst.

CO Oxidation Experiments on Single Pt Catalyst Nanoparticles. Nanoparticles in the sample region of low particle density as shown in Figure S5d were chosen to achieve well-separated (>20 pixels) diffraction-limited spots on the CCD sensor chip, using the 50× objective of the microscope. The sample stage was adjusted to align the image of the chosen nanoparticles within the view of the spectrometer slit set to a 450 μm opening. The scattered light from each nanoparticle dispersed by the grating was collected in spectral image mode with 14 s integration time and accumulated with 4 acquisitions every 60 s. The same conditions as in the ensemble CO oxidation experiment were applied to compare the two results directly. A normalized scattering spectrum from each nanoparticle was extracted and fitted according to the procedure described in the previous dark-field scattering spectroscopy method section to extract the peak position.

ASSOCIATED CONTENT

Ⓢ Supporting Information

The Supporting Information is available free of charge on the ACS Publications website at DOI: 10.1021/acsnano.9b02876.

> Drawing of the setup, hydrogen oxidation data, raw optical spectra during hydrogen oxidation, CO oxidation over a Pt nanoparticle ensemble at different temperatures, sample arrangement, second independent single-particle data set for CO oxidation (PDF)

AUTHOR INFORMATION

Corresponding Author

*E-mail: clangham@chalmers.se.

ORCID Ⓘ

Arturo Susarrey Arce: 0000-0003-2572-223X
David Albinsson: 0000-0001-7275-6921
Christoph Langhammer: 0000-0003-2180-1379

Notes

The authors declare no competing financial interest.

REFERENCES

(1) Sambur, J. B.; Chen, P. Approaches to Single-Nanoparticle Catalysis. *Annu. Rev. Phys. Chem.* **2014**, *65*, 395−422.

(2) Hansen, T. W.; Wagner, J. B. Catalysts under Controlled Atmospheres in the Transmission Electron Microscope. *ACS Catal.* **2014**, *4*, 1673−1685.

(3) Hartman, T.; Wondergem, C. S.; Kumar, N.; van den Berg, A.; Weckhuysen, B. M. Surface- and Tip-Enhanced Raman Spectroscopy in Catalysis. *J. Phys. Chem. Lett.* **2016**, *7*, 1570−1584.

(4) Karim, W.; Spreafico, C.; Kleibert, A.; Gobrecht, J.; VandeVondele, J.; Ekinci, Y.; van Bokhoven, J. A. Catalyst Support Effects on Hydrogen Spillover. *Nature* **2017**, *541*, 68.

(5) Wallin, M.; Grönbeck, H.; Spetz, A. L.; Eriksson, M.; Skoglundh, M. Vibrational Analysis of H$_2$ and D$_2$ Adsorption on Pt/SiO$_2$. *J. Phys. Chem. B* **2005**, *109*, 9581−9588.

(6) Collins, S. S. E.; Cittadini, M.; Pecharromán, C.; Martucci, A.; Mulvaney, P. Hydrogen Spillover between Single Gold Nanorods and Metal Oxide Supports: A Surface Plasmon Spectroscopy Study. *ACS Nano* **2015**, *9*, 7846−7856.

(7) Karim, W.; Kleibert, A.; Hartfelder, U.; Balan, A.; Gobrecht, J.; van Bokhoven, J. A.; Ekinci, Y. Size-Dependent Redox Behavior of Iron Observed by *In-Situ* Single Nanoparticle Spectro-Microscopy on Well-Defined Model Systems. *Sci. Rep.* **2016**, *6*, 18818.

(8) Suchorski, Y.; Kozlov, S. M.; Bespalov, I.; Datler, M.; Vogel, D.; Budinska, Z.; Neyman, K. M.; Rupprechter, G. The Role of Metal/Oxide Interfaces for Long-Range Metal Particle Activation During CO Oxidation. *Nat. Mater.* **2018**, *17*, 519−522.

(9) Mayer, K. M.; Hafner, J. H. Localized Surface Plasmon Resonance Sensors. *Chem. Rev.* **2011**, *111*, 3828−3857.

(10) Tittl, A.; Giessen, H.; Liu, N. Plasmonic Gas and Chemical Sensing. *Nanophotonics* **2014**, *3*, 157−180.

(11) Larsson, E. M.; Syrenova, S.; Langhammer, C. Nanoplasmonic Sensing for Nanomaterials Science. *Nanophotonics* **2012**, *1*, 249−266.

(12) Anker, J. N.; Hall, W. P.; Lyandres, O.; Shah, N. C.; Zhao, J.; Van Duyne, R. P. Biosensing with Plasmonic Nanosensors. *Nat. Mater.* **2008**, *7*, 442−453.

(13) Mayer, K. M.; Hafner, J. H. Localized Surface Plasmon Resonance Sensors. *Chem. Rev.* **2011**, *111*, 3828−3857.

(14) Langer, J.; Novikov, S. M.; Liz-Marzán, L. M. Sensing Using Plasmonic Nanostructures and Nanoparticles. *Nanotechnology* **2015**, *26*, 322001.

(15) Wadell, C.; Syrenova, S.; Langhammer, C. Plasmonic Hydrogen Sensing with Nanostructured Metal Hydrides. *ACS Nano* **2014**, *8*, 11925−11940.

(16) Joy, N. A.; Nandasiri, M. I.; Rogers, P. H.; Jiang, W.; Varga, T.; Kuchibhatla, S. V. N. T.; Thevuthasan, S.; Carpenter, M. A. Selective Plasmonic Gas Sensing: H_2, NO_2, and CO Spectral Discrimination by a Single Au-CeO_2 Nanocomposite Film. *Anal. Chem.* **2012**, *84*, 5025−5034.

(17) Larsson, E. M.; Langhammer, C.; Zorić, I.; Kasemo, B. Nanoplasmonic Probes of Catalytic Reactions. *Science* **2009**, *326*, 1091−1094.

(18) Langhammer, C.; Larsson, E. M. Nanoplasmonic *In Situ* Spectroscopy for Catalysis Applications. *ACS Catal.* **2012**, *2*, 2036−2045.

(19) Novo, C.; Funston, A. M.; Mulvaney, P. Direct Observation of Chemical Reactions on Single Gold Nanocrystals Using Surface Plasmon Spectroscopy. *Nat. Nanotechnol.* **2008**, *3*, 598−602.

(20) Fredriksson, H. O. A.; Larsson Langhammer, E. M.; Niemantsverdriet, J. W. Reduction of Cu-Promoted Fe Model Catalyst Studied by *In-Situ* Indirect Nanoplasmonic Sensing and X-Ray Photoelectron Spectroscopy. *J. Phys. Chem. C* **2015**, *119*, 4085−4094.

(21) Bu, Y.; Niemantsverdriet, J. W. H.; Fredriksson, H. O. A. Cu Model Catalyst Dynamics and CO Oxidation Kinetics Studied by Simultaneous *In Situ* Uv−Vis and Mass Spectroscopy. *ACS Catal.* **2016**, *6*, 2867−2876.

(22) Johánek, V.; Laurin, M.; Grant, A. W.; Kasemo, B.; Henry, C. R.; Libuda, J. Fluctuations and Bistabilities on Catalyst Nanoparticles. *Science* **2004**, *304*, 1639−1644.

(23) Alayoglu, S.; Krier, J. M.; Michalak, W. D.; Zhu, Z.; Gross, E.; Somorjai, G. A. *In Situ* Surface and Reaction Probe Studies with Model Nanoparticle Catalysts. *ACS Catal.* **2012**, *2*, 2250−2258.

(24) Hoener, B. S.; Kirchner, S. R.; Heiderscheit, T. S.; Collins, S. S. E.; Chang, W.-S.; Link, S.; Landes, C. F. Plasmonic Sensing and Control of Single-Nanoparticle Electrochemistry. *Chem.* **2018**, *4*, 1560−1585.

(25) Wang, W. Imaging the Chemical Activity of Single Nanoparticles with Optical Microscopy. *Chem. Soc. Rev.* **2018**, *47*, 2485−2508.

(26) Liu, N.; Tang, M. L.; Hentschel, M.; Giessen, H.; Alivisatos, A. P. Nanoantenna-Enhanced Gas Sensing in a Single Tailored Nanofocus. *Nat. Mater.* **2011**, *10*, 631−636.

(27) Tang, M. L.; Liu, N.; Dionne, J. A.; Alivisatos, A. P. Observations of Shape-Dependent Hydrogen Uptake Trajectories from Single Nanocrystals. *J. Am. Chem. Soc.* **2011**, *133*, 13220−13223.

(28) Syrenova, S.; Wadell, C.; Nugroho, F. A. A.; Gschneidtner, T. A.; Diaz Fernandez, Y. A.; Nalin, G.; Switlik, D.; Westerlund, F.; Antosiewicz, T. J.; Zhdanov, V. P.; Moth-Poulsen, K.; Langhammer, C. Hydride Formation Thermodynamics and Hysteresis in Individual Pd Nanocrystals with Different Size and Shape. *Nat. Mater.* **2015**, *14*, 1236−1244.

(29) McFarland, A. D.; Van Duyne, R. P. Single Silver Nanoparticles as Real-Time Optical Sensors with Zeptomole Sensitivity. *Nano Lett.* **2003**, *3*, 1057−1062.

(30) Chen, L.; Wu, B.; Guo, L.; Tey, R.; Huang, Y.; Kim, D.-H. A Single-Nanoparticle NO_2 Gas Sensor Constructed Using Active Molecular Plasmonics. *Chem. Commun.* **2015**, *51*, 1326−1329.

(31) Seo, D.; Park, G.; Song, H. Plasmonic Monitoring of Catalytic Hydrogen Generation by a Single Nanoparticle Probe. *J. Am. Chem. Soc.* **2012**, *134*, 1221−1227.

(32) Zopf, D.; Jatschka, J.; Dathe, A.; Jahr, N.; Fritzsche, W.; Stranik, O. Hyperspectral Imaging of Plasmon Resonances in Metallic Nanoparticles. *Biosens. Bioelectron.* **2016**, *81*, 287−293.

(33) Fritzsche, J.; Albinsson, D.; Fritzsche, M.; Antosiewicz, T. J.; Westerlund, F.; Langhammer, C. Single Particle Nanoplasmonic Sensing in Individual Nanofluidic Channels. *Nano Lett.* **2016**, *16*, 7857−7864.

(34) Pini, V.; Kosaka, P. M.; Ruz, J. J.; Malvar, O.; Encinar, M.; Tamayo, J.; Calleja, M. Spatially Multiplexed Dark-Field Microspectrophotometry for Nanoplasmonics. *Sci. Rep.* **2016**, *6*, 22836.

(35) Alekseeva, S.; Fanta, A. B. d. S.; Iandolo, B.; Antosiewicz, T. J.; Nugroho, F. A. A.; Wagner, J. B.; Burrows, A.; Zhdanov, V. P.; Langhammer, C. Grain Boundary Mediated Hydriding Phase Transformations in Individual Polycrystalline Metal Nanoparticles. *Nat. Commun.* **2017**, *8*, 1084.

(36) Taylor, A. B.; Zijlstra, P. Single-Molecule Plasmon Sensing: Current Status and Future Prospects. *ACS Sens* **2017**, *2*, 1103−1122.

(37) Li, K.; Qin, W.; Xu, Y.; Peng, T.; Li, D. Optical Approaches in Study of Nanocatalysis with Single-Molecule and Single-Particle Resolution. *Front. Optoelectron.* **2015**, *8*, 379−393.

(38) Li, K.; Wang, K.; Qin, W.; Deng, S.; Li, D.; Shi, J.; Huang, Q.; Fan, C. DNA-Directed Assembly of Gold Nanohalo for Quantitative Plasmonic Imaging of Single-Particle Catalysis. *J. Am. Chem. Soc.* **2015**, *137*, 4292−4295.

(39) Huang, J.; Zhu, Y.; Lin, M.; Wang, Q.; Zhao, L.; Yang, Y.; Yao, K. X.; Han, Y. Site-Specific Growth of Au−Pd Alloy Horns on Au Nanorods: A Platform for Highly Sensitive Monitoring of Catalytic Reactions by Surface Enhancement Raman Spectroscopy. *J. Am. Chem. Soc.* **2013**, *135*, 8552−8561.

(40) Eo, M.; Baek, J.; Song, H. D.; Lee, S.; Yi, J. Quantification of Electron Transfer Rates of Different Facets on Single Gold Nanoparticles During Catalytic Reactions. *Chem. Commun.* **2013**, *49*, 5204−5206.

(41) Wonner, K.; Evers, M. V.; Tschulik, K. Simultaneous Opto- and Spectro-Electrochemistry: Reactions of Individual Nanoparticles Uncovered by Dark-Field Microscopy. *J. Am. Chem. Soc.* **2018**, *140*, 12658−12661.

(42) Grote, J.; Dankbar, N.; Gedig, E.; Koenig, S. Surface Plasmon Resonance/Mass Spectrometry Interface. *Anal. Chem.* **2005**, *77*, 1157−1162.

(43) Anker, J. N.; Hall, W. P.; Lambert, M. P.; Velasco, P. T.; Mrksich, M.; Klein, W. L.; Van Duyne, R. P. Detection and Identification of Bioanalytes with High Resolution LSPR Spectroscopy and MALDI Mass Spectrometry. *J. Phys. Chem. C* **2009**, *113*, 5891−5894.

(44) Langhammer, C.; Larsson, E. M.; Kasemo, B.; Zorić, I. Indirect Nanoplasmonic Sensing: Ultrasensitive Experimental Platform for Nanomaterials Science and Optical Nanocalorimetry. *Nano Lett.* **2010**, *10*, 3529−3538.

(45) Langhammer, C.; Kasemo, B.; Zoric, I. Absorption and Scattering of Light by Pt, Pd, Ag, and Au Nanodisks: Absolute Cross Sections and Branching Ratios. *J. Chem. Phys.* **2007**, *126*, 194702.

(46) Zhang, C.; Zhao, H.; Zhou, L.; Schlather, A. E.; Dong, L.; McClain, M. J.; Swearer, D. F.; Nordlander, P.; Halas, N. J. Al−Pd Nanodisk Heterodimers as Antenna−Reactor Photocatalysts. *Nano Lett.* **2016**, *16*, 6677−6682.

(47) Syrenova, S.; Wadell, C.; Langhammer, C. Shrinking-Hole Colloidal Lithography: Self-Aligned Nanofabrication of Complex Plasmonic Nanoantennas. *Nano Lett.* **2014**, *14*, 2655−2663.

(48) Imbihl, R.; Ertl, G. Oscillatory Kinetics in Heterogeneous Catalysis. *Chem. Rev.* **1995**, *95*, 697−733.

(49) Zhdanov, V. P.; Kasemo, B. Kinetic Phase Transitions in Simple Reactions on Solid Surfaces. *Surf. Sci. Rep.* **1994**, *20*, 113−189.

(50) Kasemo, B. Quartz Tube Orifice Leaks for Local, Fast-Response Gas Sampling to Mass Spectrometers. *Rev. Sci. Instrum.* **1979**, *50*, 1602−1604.

(51) Shegai, T.; Langhammer, C. Hydride Formation in Single Palladium and Magnesium Nanoparticles Studied by Nanoplasmonic Dark-Field Scattering Spectroscopy. *Adv. Mater.* **2011**, *23*, 4409−4414.

(52) Nugroho, F. A. A.; Iandolo, B.; Wagner, J. B.; Langhammer, C. Bottom-Up Nanofabrication of Supported Noble Metal Alloy Nanoparticle Arrays for Plasmonics. *ACS Nano* **2016**, *10*, 2871−2879.

(53) Ponec, V.; Bond, G. C. *Catalysis by Metals and Alloys*; Elsevier: Amsterdam, 1995; Vol. *95*, p 744.

(54) van Spronsen, M. A.; Frenken, J. W. M.; Groot, I. M. N. Surface Science under Reaction Conditions: CO Oxidation on Pt and Pd Model Catalysts. *Chem. Soc. Rev.* **2017**, *46*, 4347−4374.

(55) van Spronsen, M. A.; Frenken, J. W. M.; Groot, I. M. N. Observing the Oxidation of Platinum. *Nat. Commun.* **2017**, *8*, 429.

(56) Vendelbo, S. B.; Elkjær, C. F.; Falsig, H.; Puspitasari, I.; Dona, P.; Mele, L.; Morana, B.; Nelissen, B. J.; van Rijn, R.; Creemer, J. F.; Kooyman, P. J.; Helveg, S. Visualization of Oscillatory Behaviour of Pt Nanoparticles Catalysing CO Oxidation. *Nat. Mater.* **2014**, *13*, 884−890.

(57) Hartmann, N.; Imbihl, R.; Vogel, W. Experimental Evidence for an Oxidation/Reduction Mechanism in Rate Oscillations of Catalytic CO Oxidation on Pt/SiO$_2$. *Catal. Lett.* **1994**, *28*, 373−381.

(58) Vogel, D.; Spiel, C.; Suchorski, Y.; Trinchero, A.; Schlögl, R.; Grönbeck, H.; Rupprechter, G. Local Catalytic Ignition During Co Oxidation on Low-Index Pt and Pd Surfaces: A Combined Peem, Ms, and Dft Study. *Angew. Chem., Int. Ed.* **2012**, *51*, 10041−10044.

(59) Wickman, B.; Fredriksson, H.; Gustafsson, S.; Olsson, E.; Kasemo, B. Fabrication of Poly- and Single-Crystalline Platinum Nanostructures Using Hole-Mask Colloidal Lithography, Electrodeposition and Annealing. *Nanotechnology* **2011**, *22*, 345302.

(60) Fredriksson, H.; Alaverdyan, Y.; Dmitriev, A.; Langhammer, C.; Sutherland, D. S.; Zaech, M.; Kasemo, B. Hole-Mask Colloidal Lithography. *Adv. Mater.* **2007**, *19*, 4297−4302.

(61) Aćimović, S. S.; Šípová-Jungová, H.; Emilsson, G.; Shao, L.; Dahlin, A. B.; Käll, M.; Antosiewicz, T. J. Antibody−Antigen Interaction Dynamics Revealed by Analysis of Single-Molecule Equilibrium Fluctuations on Individual Plasmonic Nanoparticle Biosensors. *ACS Nano* **2018**, *12*, 9958−9965.

(62) Henriksen, T. R.; Olsen, J. L.; Vesborg, P.; Chorkendorff, I.; Hansen, O. Highly Sensitive Silicon Microreactor for Catalyst Testing. *Rev. Sci. Instrum.* **2009**, *80*, 124101.

(63) Kelly, K. L.; Coronado, E.; Zhao, L. L.; Schatz, G. C. The Optical Properties of Metal Nanoparticles: The Influence of Size, Shape, and Dielectric Environment. *J. Phys. Chem. B* **2003**, *107*, 668−677.

(64) Chen, P.-C.; Liu, X.; Hedrick, J. L.; Xie, Z.; Wang, S.; Lin, Q.-Y.; Hersam, M. C.; Dravid, V. P.; Mirkin, C. A. Polyelemental Nanoparticle Libraries. *Science* **2016**, *352*, 1565−1569.

(65) Hovel, H.; Fritz, S.; Hilger, A.; Kreibig, U.; Vollmer, M. Width of Cluster Plasmon Resonances - Bulk Dielectric Function and Chemical Interface Damping. *Phys. Rev. B: Condens. Matter Mater. Phys.* **1993**, *48*, 18178−18188.

(66) Rioux, D.; Vallières, S.; Besner, S.; Muñoz, P.; Mazur, E.; Meunier, M. An Analytic Model for the Dielectric Function of Au, Ag, and Their Alloys. *Adv. Opt. Mater.* **2014**, *2*, 176−182.

(67) Nguyen, N. L.; de Gironcoli, S.; Piccinin, S. Ag-Cu Catalysts for Ethylene Epoxidation: Selectivity and Activity Descriptors. *J. Chem. Phys.* **2013**, *138*, 184707.

(68) Nugroho, F. A. A.; Darmadi, I.; Cusinato, L.; Susarrey-Arce, A.; Schreuders, H.; Bannenberg, L. J.; da Silva Fanta, A. B.; Kadkhodazadeh, S.; Wagner, J. B.; Antosiewicz, T. J.; Hellman, A.; Zhdanov, V. P.; Dam, B.; Langhammer, C. Metal−Polymer Hybrid Nanomaterials for Plasmonic Ultrafast Hydrogen Detection. *Nat. Mater.* **2019**, *18*, 489−495.

(69) Hanarp, P.; Sutherland, D. S.; Gold, J.; Kasemo, B. Control of Nanoparticle Film Structure for Colloidal Lithography. *Colloids Surf., A* **2003**, *214*, 23−36.